PHYSICAL REVIEW ACCELERATORS AND BEAMS **28,** 090102 (2025)

Time-resolved space-charge compensation studies for pulsed and matched proton beam in a low-energy transport line

Emre Cosgun and Min Sup Hur
*Department of Physics, Ulsan National Institute of Science and Technology,
Ulsan 44919, Republic of Korea*

Seokho Moon and Donghwan Kim
*Korea Multi-purpose Accelerator Complex, Korea Atomic Energy Research Institute,
Gyeongju 38180, Republic of Korea*

Moses Chung[*]
*Department of Physics and Division of Advanced Nuclear Engineering,
Pohang University of Science and Technology, Pohang 37673, Republic of Korea*

(Received 24 January 2025; accepted 4 September 2025; published 25 September 2025)

In low-energy beam transport of pulsed, high-perveance ion beams operating under neutralized space-charge conditions, understanding the time required for the compensation process to develop—known as the build-up time—is critically important for ensuring efficient beam transmission and maintaining beam quality. This study presents a comprehensive investigation into the dynamics and optimization of space-charge compensation (SCC) in the low-energy beam transport line of a high-perveance proton beam, integrating numerical simulations with time-resolved experimental measurements. A detailed 3D numerical simulation has been developed, which takes into account both secondary electron and ion dynamics to evaluate the temporal evolution of the beam potential and its dependence on various parameters. Additionally, experimental measurements complement the numerical results, providing validation of SCC dynamics. These measurements analyze the effects of injected gas properties, pressure levels, and beam current on build-up time, while also considering nonlinear space-charge effects that influence SCC efficiency and the beam's transverse emittance evolution. A correlation between SCC and radio-frequency quadrupole matching conditions is also examined, demonstrating the necessity of adjusting solenoid magnet settings to maintain optimal transmission efficiency.

DOI: 10.1103/l8v5-ch9z

I. INTRODUCTION

In recent years, there has been a significant rise in high-power accelerators capable of delivering megawatt-level outputs. A critical challenge in these systems is managing the extraction and transport of the charged particles while controlling emittance growth within the low-energy beam transport (LEBT) line, where space-charge forces dominate. Analyzing beam behavior requires accounting not only for space-charge effects but also for the compensation of this charge, which arises from interactions with the residual gas surrounding the beam. Space-charge compensation (SCC) is thus essential for preserving beam quality and limiting emittance growth during low-energy, high-intensity beam transport. As reported in Refs. [1,2], injecting krypton or argon gas can reduce beam emittance by a factor of 3 with only a 5% loss of beam current.

Transport of pulsed high-perveance space-charge-compensated ion beams requires an understanding of the compensation build-up time. Time-resolved measurements of the compensation process have been performed to measure the electric potential distribution as a function of time [3–5], and it is found that the theoretically estimated rise time of space-charge compensation is shorter than the experimental build-up time. This discrepancy arises primarily due to electron losses, which extend the build-up time and may prevent complete space-charge neutralization. The degree of compensation achieved is governed by the dynamic equilibrium between electron production and loss mechanisms [6].

The effective operation of the LEBT line, on the other hand, critically depends on the rate and efficiency of space-charge neutralization. For minimizing focusing gradients and

---

[*] Contact author: moses@postech.ac.kr

particle losses, it is highly desirable to maintain a sufficient level of neutralization throughout the entire system. Several factors contribute to the compensation degree, including the level of the beamline pressure, the beam currents, the beam energy, and the size of the beam [7–10].

The space charge of an ion beam can be neutralized through two main methods [11]. The first method is self-compensation (or gas compensation), which occurs when the ion beam passes through a low-pressure line, ionizing atoms within the gas. These gas sources include residual gases composed of small amounts of air from vacuum leaks, operating gases diffused from the ion source, and additionally injected inert gases such as krypton, argon, and neon. Among these gases, argon and krypton are used more frequently due to their higher ionization cross sections and lower ionization potentials compared to neon. The ionization process generates charges that naturally compensate for the space charge of the ion beam. The second one is forced compensation, where external charges are introduced into the beam by superimposing the ion beam onto a preexisting, accelerated beam of particles with the opposite charge [12–16]. In this study, we will focus on the first method, accounting for secondary ions and electrons when beam ions pass through inserted gases.

This study presents a comprehensive investigation into SCC dynamics, combining advanced three-dimensional numerical simulations with time-resolved experimental measurements to analyze how gas pressure level, gas species, beam current, and beam size influence SCC build-up time and compensation efficiency. We also aim to explain the differences observed between simulation and experimental SCC build-up times by considering possible physical mechanisms such as secondary ion and electron dynamics, as well as experimental uncertainties.

We propose the numerical calculation of the space-charge compensation model of the proton beam through a detailed simulation approach in three stages, followed by experimental validation. The `first stage` of the simulation involves calculating the trajectory of the beam and its self-potential. This step establishes the foundation of space-charge densities by calculating the beam potential in the absence of external electric fields, allowing the space-charge densities to be saved for the next step.

In the `second stage`, the space-charge compensation process is modeled by introducing secondary particles into the system. These secondaries, which include ions and electrons, are iteratively added to the simulation, allowing the space-charge densities to evolve cumulatively over time. The simulation tracks the temporal evolution of space-charge densities until a steady state is reached, enabling a detailed analysis of the build-up time and the dynamics of compensation under varying gas pressures and types.

The `third stage` evaluates beam parameters under the influence of neutralized space charge. This stage assesses the effectiveness of the compensation mechanisms by examining key parameters, including beam emittance, rms size, radio-frequency quadrupole (RFQ) transmission efficiency, and phase-space distribution.

Phase-space distribution measurements of the beam are conducted using Allison-type emittance scanners [17]. During the measurement period, we investigated the effects of varying injected pressure levels, gas species, and beam parameters such as beam current on the SCC build-up time. Additionally, we studied the impact of nonlinear space-charge effects on beam dynamics and the evolution of beam emittance quality. Furthermore, we examined the matching conditions and RFQ transmission under different SCC conditions to ensure efficient injection into the RFQ.

II. METHODS AND SETUP

A. Physics of space-charge compensation

The generalized perveance, denoted by K, measures the strength of space charge [18],

$$K = \frac{qI(1-\gamma^2\eta(t))}{2\pi\epsilon_0 m\gamma^3\beta^3}, \tag{1}$$

where q, I, ϵ_0, and m are the charge, current, vacuum permittivity, and rest mass, respectively. The terms γ and β represent the relativistic parameters of the particle beam. The parameter $\eta(t)$ is the space-charge compensation factor, with a higher $\eta(t)$ indicating a lower space-charge strength. If we define ϕ_c as the beam potential on the axis, the SCC degree during the build-up time is given by

$$\eta(t) = 1 - \frac{\phi_{\text{total}}(t)}{\phi_c}, \tag{2}$$

where $\phi_{\text{total}}(t) = \phi_c + \phi_{\text{ion}}(t) + \phi_{\text{electron}}(t)$ is the total potential of the beam and secondaries on axis. Here, $\phi_{\text{ion}}(t)$ and $\phi_{\text{electron}}(t)$ represent the potentials due to ions and electrons, respectively. At steady state, when all secondary ions are assumed to be expelled to the wall, Eq. (2) is written as $\eta(\tau_{\text{SCC}}) = 1 - \phi_{\text{total}}(\tau_{\text{SCC}})/\phi_c$ where τ_{SCC} is the characteristic time of the compensation.

When an ion beam travels through the residual gas in an accelerator system, it ionizes the neutral atoms. The resulting electrons gather in the space-charge potential of the positive ion beam and neutralize the positive space charge. The positive residual gas ions are then accelerated towards the beam pipe wall [19]. The general equation for proton impact ionization can be written as

$$\text{H}^+ + \text{X} \rightarrow \text{H}^+ + \text{X}^+ + e^-, \tag{3}$$

where X indicates residual or injected gas. Due to their different cross sections, we consider two injected gases here; krypton and argon, and cross-section data are available for proton beams with an energy of 25 keV for these gaseous targets [20,21]. The electrons released during impact ionization exhibit a broad energy distribution, which influences the modeling of space-charge compensation. A detailed derivation of the maximum energy transfer and resulting free-electron energy distribution is provided in the Appendix.

The number of secondary electrons and ions produced per unit volume per unit of time is given by

$$\frac{dn_e}{dt} = n_b \vartheta_b n_a \sigma_e, \tag{4a}$$

$$\frac{dn_i}{dt} = n_b \vartheta_b n_a \sigma_i, \tag{4b}$$

where n_b, n_e, and n_i are beam, electron, and ion densities, respectively, ϑ_b is beam velocity, n_a is gas density, and σ_e and σ_i are electron production and ion production cross sections. Since only ionization is being taken into account, we can consider $\sigma_e = \sigma_i$. The rate of production of electrons and residual gas ions determines the characteristic time of the compensation, and of course, taking the ion production rate into account makes the compensation time much longer. When ions are completely expelled from the beam, then we can write as follows:

$$\frac{dn_e}{dt} = \frac{n_b}{\tau_{\mathrm{SCC}}}. \tag{5}$$

B. Experimental apparatus

The numerical calculations and phase-space measurements are performed for the proton beam at the 1 MeV/n RFQ Beam Test Stand (BTS) in the Korea Multi-purpose Accelerator Complex (KOMAC) [22]. The 2.4 m length BTS LEBT line has been commissioned for 25 keV proton beam generated from the 2.45 GHz microwave ion source, as illustrated in Fig. 1. The vacuum chamber inner diameter is approximately 150 mm. The proton beam is matched to the RFQ by employing two solenoid magnets. A diagnostic chamber called the “9-port diagnostic box” is positioned approximately 1.2 m downstream from the ion source, between the two solenoids. This box has a rectangular dimension of 300 mm × 300 mm × 500 mm and houses two Allison scanners that measure the transverse phase-space distribution in both horizontal and vertical planes. In addition to the Allison scanners, the diagnostic box is equipped with a vacuum gauge for monitoring total pressure during gas injection, as well as a turbomolecular pump for maintaining vacuum conditions. Two steering magnets are installed upstream and downstream of the diagnostic box to tune the beam trajectory prior to emittance measurements. Krypton and argon gases are injected separately, immediately after the ion source. To monitor the beam current, two ac current transformers (ACCTs) are installed along the LEBT: one located just exit of the ion source and the other positioned entrance of the RFQ.

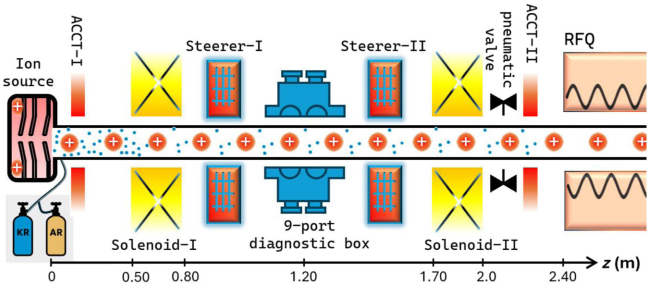

FIG. 1. Schematic diagram of BTS LEBT line.

III. MODELING AND SIMULATIONS

Several sophisticated numerical calculations [23–28] are available for both negative and positive beam compensation models to estimate build-up time and compensation degree. We chose a dedicated ion optical code IBSimu [29] to construct the SCC model, which is capable of solving electric fields in one-dimensional, two-dimensional (planar or cylindrical symmetry), or full three-dimensional simulation geometries. Furthermore, it is straightforward to sum up the space-charge densities of the ion beam and the created secondaries in the IBSimu, which is the principle of the SCC model in this study.

Referring to Sec. I, our investigation of the model comprises three stages: depositing the space charge of the beam by solving the field distribution, modeling the SCC process under this beam space-charge density, and investigating the evolution of beam parameters during the build-up and after reaching the steady state of SCC.

A. Self-potential of beam

1. Geometry, boundary conditions

The length of the LEBT line is almost 2.4 m, and the chamber diameter is specified. The boundary condition of the model $\phi(z = 0) = \phi(z = L) = 0$ applies to the LEBT line, which is excluded from both the ion source and RFQ. Here, L represents the length of the beamline. Since the line has two solenoid magnets, the 3D field map of magnets is imported, and the magnetic flux density of each solenoid is finely tuned to ensure that the beam is properly matched.

2. Initial beam distribution

At the start of the LEBT line, the extracted 4D beam distribution from the ion source, which represents the initial conditions of the beam in terms of position and momentum, is initiated. The ion source is equipped with a three-electrode extraction configuration. The plasma electrode with a 6 mm aperture is employed to extract a proton beam with an energy of 25 keV. It is known that other molecular ions, such as H_2^+ and H_3^+, are also extracted from the ion source and may represent a significant fraction of the beam. However, in this study, we focus just on the proton beam and do not include these molecular ions in the model.

3. Line potential and trajectories

To begin the simulation, the Laplace equation $\nabla^2\phi = 0$ is solved in the absence of space charge and the electric field $\mathbf{E}$ is calculated, which will influence the motion of the particles within the beam. The beam particle trajectories are computed, and based on the current positions of the particles, the charge density ρ_b of the beam is deposited onto the mesh grid. This updated charge distribution is then used to solve the Poisson equation $\nabla^2\phi = -\rho_b/\epsilon_0$, giving a new potential distribution. The updated fields are used to retrace particle trajectories. This iterative process continues until convergence is achieved. The final beam distribution is shown in Fig. 2. The self-potential of the matched beam is given in Fig. 3 for different beam current levels. It is clear that an increased beam charge density leads to an increased space- charge potential.

B. SCC modeling

In this section, we aim to model the dynamic behavior of the SCC process for a matched proton beam as it travels through a medium with varying injected krypton and argon gas pressures. Only ionization is considered for secondary charge accumulation, and charge exchange or surface production is ignored.

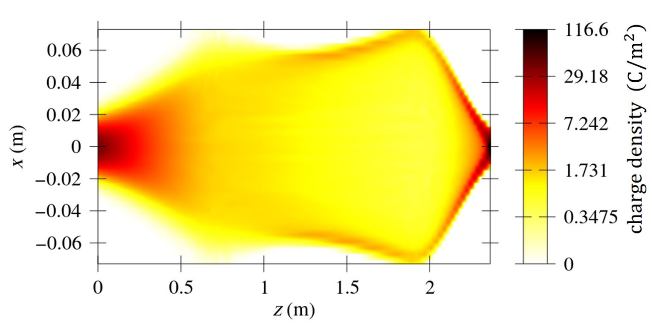

FIG. 2. Space-charge density of proton beam in LEBT. The solenoid strengths are adjusted to match the beam to RFQ.

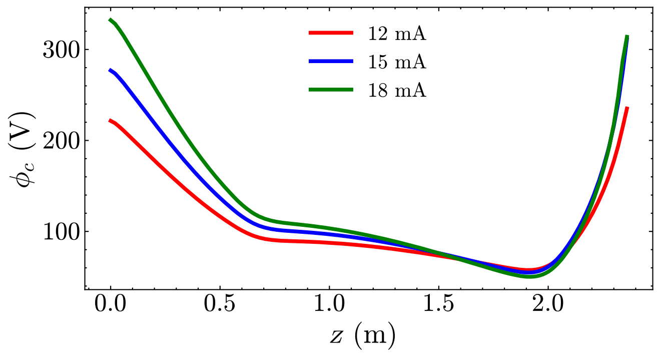

FIG. 3. Line potential of beam with different space charges.

The process begins with uploading the beam's charge density map ρ_b, which is solved in Sec. III A.

The next step involves the Monte Carlo generator, which simulates the production of secondary particles by modeling the probabilistic interactions of primary particles with the target gas. Each time step (Δt), a certain number of secondary particles, determined by Eq. (4), are generated randomly. The time step is determined based on the velocity of the fastest secondary particles and must be small enough to prevent them from crossing more than one grid cell during a single time step. It is given by the formula $\Delta t = h/v_{\mathrm{max}}$, where h is the spatial mesh size and v_{max} represents the maximum particle velocity, which in this case is the electron velocity. For the beam with 15 mA current and 25 keV energy, free-fall electrons are rapidly accelerated by the beam potential, reaching velocities of approximately 2×10^6 m/s. This result allows us to estimate the appropriate Δt. A reasonable value for the time step is around 1×10^{-9} s to maintain numerical stability.

As discussed in Eq. (A5) in the Appendix, the estimated electron velocities resulting from ionization by a 25 keV proton beam are approximately 3.69×10^6 m/s for argon and 3.76×10^6 m/s for krypton. To explore how initial electron energy affects the SCC dynamics, we conducted a comparison using two representative cases: one assuming electrons are initialized at rest ($v_e = 0$ m/s), and the other assigning electrons an initial velocity of 3×10^6 m/s, consistent with analytical estimates based on impact ionization energy. In this analysis, only electrons are included as secondary particles, and ions are intentionally excluded to isolate the effect of electron dynamics. The results clearly indicate that assigning higher initial velocities leads to a slower build-up of space-charge compensation and a reduced compensation degree. This behavior arises because faster electrons, having higher kinetic energy, are more likely to escape the beam potential rather than being trapped, thereby reducing their role in neutralizing the beam's space charge.

Once the secondary particles are added, the system is stepped forward in time. In every step, the trajectory of these particles is saved for the next step to ensure continuity in the calculation. Once the total charge density is updated with contributions from the secondaries, the Poisson equation $\nabla^2\phi = -(\rho_b - \rho_e + \rho_i)/\epsilon_0$ is solved again, this time accounting for the charge densities of secondary electrons, ρ_e, and the secondary ions ρ_i. This recalculation updates the electric potential, ϕ, which determines the electric field that influences the particle trajectories in the next time step. After every change in the charge distribution, the electric potential is recalculated. As a result, the accumulation of charge density of secondary particles modifies the beam charge density until the total charge density reaches a steady state. Throughout this process,

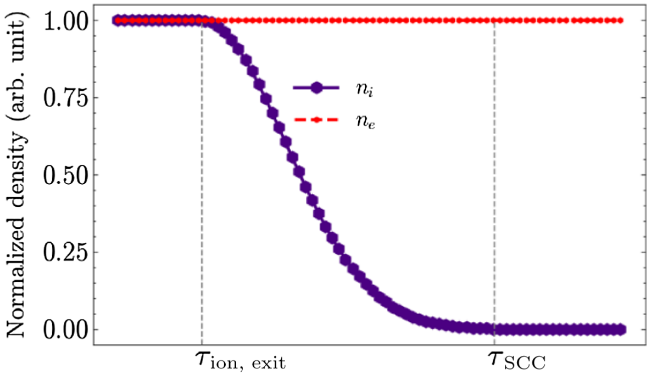

FIG. 4. The model description of secondaries over time.

the gas pressure is assumed to be uniform across the entire beamline.

The dynamics of secondary ions require special attention, especially when estimating their exit time from the beam. When secondary ions are introduced into the model, their behavior is primarily governed by the beam's electric field. Secondary ions are repelled radially outward from the beam due to the electrostatic potential of the beam itself. The characteristic velocity of ions under the free fall in the beam potential is

$$v_i = \frac{\sqrt{\Delta V_b}}{\sqrt{2m_i/q_i}}, \tag{6}$$

where ΔV_b is the potential difference of the beam center and edge, m_i and q_i are the ion mass and charge, respectively. The time needed for an ion to be repelled from the beam with respect to the beam radius (R_b) is defined as [24]:

$$\tau_{\text{ion,exit}} = R_b\sqrt{\frac{m_i/q_i}{\Delta V_b}}. \tag{7}$$

When considering a uniform beam, estimating the ion exit time is relatively straightforward because the velocity distribution of ions can be averaged, and the ion exit time can be estimated using Eq. (7). However, in the case of the matched beam shown in Fig. 2, the created ions experience a highly varying potential along the beam propagation direction (see Fig. 3). As a result, their velocity distribution exhibits significant statistical spread due to the nonuniform potential field. In this scenario, we need to construct a model that focuses on the dynamics of the fastest ions in the beam because they are the first to respond to the beam's potential and exit the compensation region. These ions must achieve their highest velocity at the center of the beam, where the potential difference, as defined in Eq. (6), is the greatest. Figure 4 illustrates the model to describe the time evolution of normalized ion and electron densities during secondary particle production. $\tau_{\text{ion,exit}}$ corresponds to the moment when ions start exiting the beam. For a proton beam with an energy of 25 keV and a current of 15 mA, the maximum observed ion velocity is approximately 2×10^4 m/s, leading to an ion exit time $\tau_{\text{ion,exit}}$ of about 1 μs. The gradual reduction in ion density indicates that the slower ions steadily leave the beam. As the ions exit the beam, total density decreases, allowing for compensation by the captured electrons, eventually leading the system to reach a steady state, and τ_{SCC} represents that point. Here, the value of τ_{SCC} is determined by the residual gas pressure and the type of injected gas.

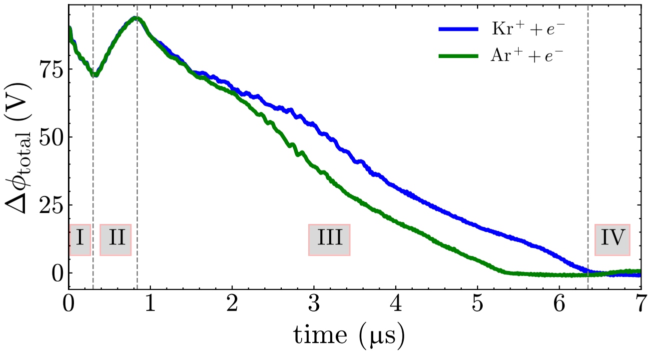

FIG. 5. Simulated evolution of the beam potential with equal secondary production rate (at pressure level $p_{\text{Ar}} > p_{\text{Kr}}$) over time for two gases. The purpose of this figure is not to compare the efficiency of krypton and argon directly but to focus on how secondary ions behave under the same beam potential conditions.

Figure 5 illustrates the time evolution of the total beam potential $\Delta\phi_{\text{total}}$, specifically at the position between the two solenoid magnets shown in Fig. 3, where the Allison scanner is installed. In this study, all evaluations of beam potential, beam size, transmission, and emittance over time are conducted at the same location within the LEBT line. The highlighting of different regions (I–IV) corresponds to distinct phases of secondary electron and ion dynamics when different gas species are injected. Since the ionization cross sections of Kr and Ar gases are different, achieving the same production rate requires a higher pressure for Ar^+ than for Kr^+ ($p_{\text{Ar}} > p_{\text{Kr}}$), which allows for a consistent comparison of the secondary ion velocities. On the other hand, since the production rate of the secondaries is relatively high, the stabilization time shown in the figure is not realistic, as the assumed pressure level can be considered extremely high.

Region I is the initial phase, and the secondary electrons play the dominant role. Due to their lower mass and higher mobility, the secondary electrons rapidly accumulate near the beam, reducing the beam potential. Figure 6 shows the charge density of secondary particles corresponding to the outlined regions of Fig. 5. In this region, as shown in Fig. 6(a), electrons are driving the system's early behavior.

In *Region II*, secondary ions start to accumulate in the beam. Their presence causes the potential to increase,

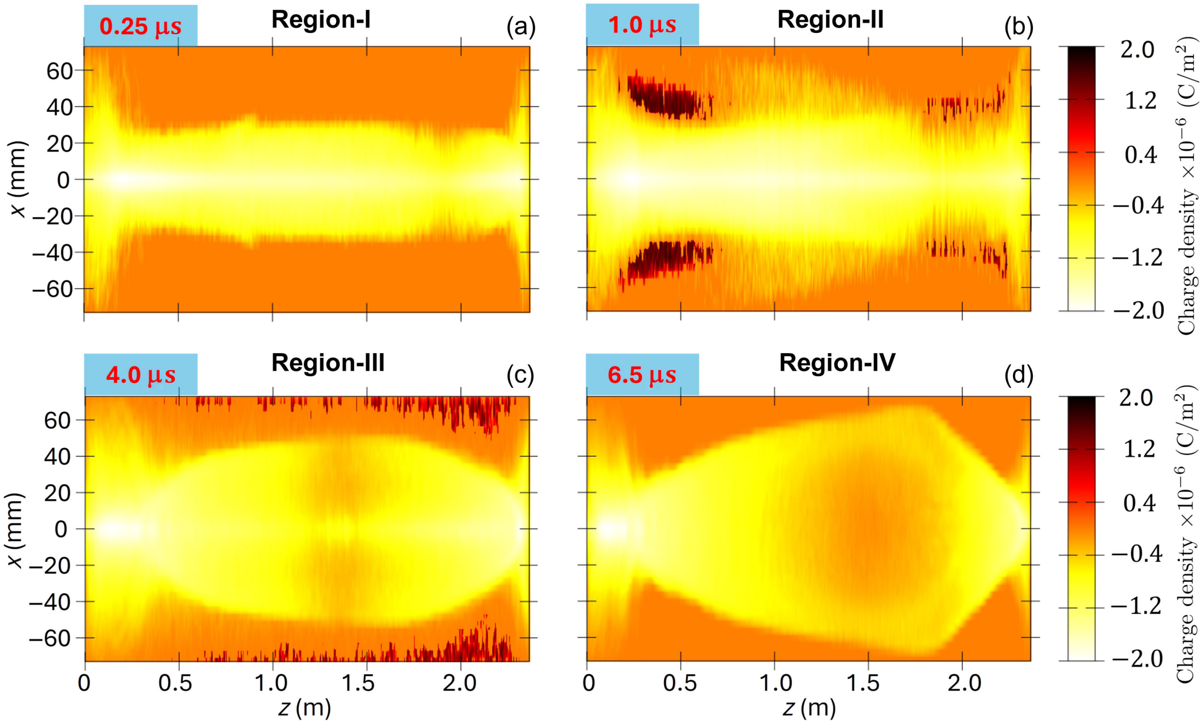

FIG. 6. Charge density of secondary particles in different phases of the SCC model. Panels (a), (b), (c), and (d) correspond to snapshots at 0.25, 1.0, 4.0, and 6.5 μs, respectively. Both electrons and ions are visible in (b) and (c), whereas (a) and (d) display only electrons. The color bar indicates the charge density of particles, with negative values representing electrons and positive values representing ions. Neutral regions are shown in orange, ion-dominated (positive) regions in red, and electron-dominated (negative) regions ranging from yellow to white.

counteracting the neutralizing effect of the electron as the ions begin to gather within the beam's electrostatic field. The peak in the potential profile corresponds to the ion exit time, $\tau_{\mathrm{ion,exit}}$, shown in Fig. 4, and is primarily governed by the fastest secondary ions. Figure 6(b) illustrates both electron and ion charge densities. Since the ions witness higher potential differences and move much faster in the high-density regions of the line during the early phase of repulsion, they become initially visible.

After reaching its peak potential, *Region III* involves the radial expulsion of ions from the beam. During this stage, the repulsion of ions from the beam, combined with the confinement of electrons within it, leads to a gradual reduction of the overall space charge, resulting in a decrease in beam potential. It appears that Ar^+ ions, having a smaller mass, are expelled more quickly under the influence of the same beam's potential compared to the heavier Kr^+ ions. The expulsion process is illustrated in Fig. 6(c), which shows ions being repelled radially from the beam while electrons remain confined within it, contributing to the stabilization of the space charge.

Finally, in *Region IV*, only electrons are present in the model. All the ions have been expelled from the beam, leaving the electrons to fully neutralize the space charge of the beam. At this stage, the system reaches a steady state condition, where the SCC is complete. This stage is depicted in Fig. 6(d). We infer that electron trajectories resemble the beam trajectories, suggesting that the electrons are thoroughly captured along the entire length of the beam and the higher beam's space-charge region captures more electrons. Notably, at steady state, the system achieves dynamic equilibrium: the rate of electron production equals the rate of electron escape from the model. This equilibrium ensures that the degree of neutralization remains constant.

1. Gas type and pressure dependence

Once the evolution of the beam potential is understood, the next step is to investigate the beam's behavior under different pressure levels of injected gas. The production rate of secondaries, referring to Eq. (4), is defined depending on different gas types and pressures. Figure 7 illustrates the time evolution of the accumulative beam potential $\Delta\phi_{\mathrm{total}}$ when krypton is injected at different pressures. At $t = 0$, the beam potential is at a high value (around 80 V), corresponding to the uncompensated beam's space charge. The rate of potential decrease depends on the pressure of krypton gas. Higher pressures (e.g., 8×10^{-5} mbar) result in faster compensation due to more secondary particles being generated and electrons being quickly captured by the beam's potential well. $\Delta\phi_{\mathrm{total}} = 0$ indicates the beam

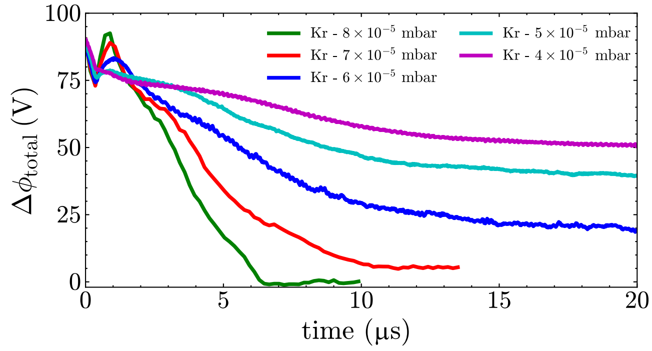

FIG. 7. Beam potential evolution with the injected krypton gas at different pressure levels.

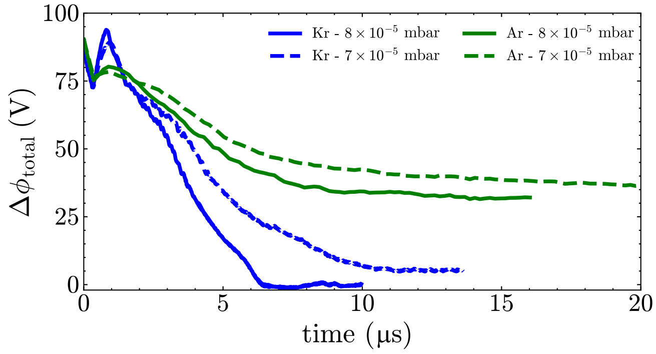

FIG. 8. Comparison of beam potential changes considering two injected gases at two different pressures.

has been fully compensated, and the SCC degree remains stable at that point.

Figure 8 compares the time evolution of the beam potential for two different gases at various pressures. The results illustrate how the type of residual gas and its pressure significantly affect the time required for the characteristic of the compensation. The key observation is that at the same pressure level, krypton results in a faster potential drop than argon, suggesting that krypton enhances SCC efficiency more effectively.

2. *Beam current effect*

Figure 9 illustrates the time-dependent evolution of the beam potential for beam currents of 12, 15, and 18 mA following the injection of constant level krypton gas. The results indicate how beam current affects the SCC process and the time needed to reach a steady state. It is seen that the initial potential is much higher due to the higher space charge (e.g., ∼100 V for the 18 mA beam and ∼85 V for the 15 mA beam). Higher beam currents result in a quicker accumulation of secondary electrons and ions compared to lower currents. The stronger potential difference gives the ions a higher velocity, allowing them to accumulate and expel more rapidly, and reducing the build-up time. Furthermore, in the second phase of SCC, the accumulation of secondary ions becomes dominant, temporarily increasing the beam potential to a peak value. For higher beam currents, this peak is more pronounced due to the higher secondary production rate.

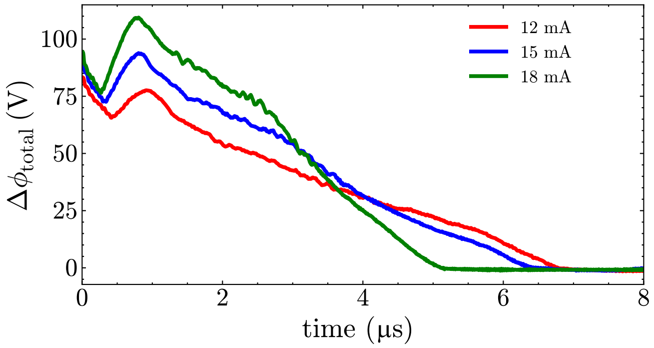

FIG. 9. Simulated evolution of the beam potential over time for different beam currents.

3. *SCC degree along the beamline*

It is straightforward to evaluate the SCC degree along the beamline in terms of Eq. (2) at the steady state condition. Figure 10 illustrates the SCC degree as a function of the longitudinal position along the beamline for injected krypton gas at different pressures (8×10^{-5}, 7×10^{-5}, and 6×10^{-5} mbar). At 8×10^{-5} mbar, the SCC degree is the highest, approaching complete compensation along most of the beamline. This indicates that the beam's space charge is nearly fully neutralized at higher gas pressures. This analysis demonstrates that the SCC degree strongly depends on the gas pressure and varies along the beamline.

4. *SCC degree at the RFQ cone region*

At the end of the LEBT, the RFQ's electric field tends to penetrate through the injection hole, significantly affecting the SCC by attracting neutralizing particles [30]. Therefore, using an electrode structure between the transition area between LEBT and RFQ, such as the RFQ repeller shown in Fig. 11, is an effective method to prevent neutralizing

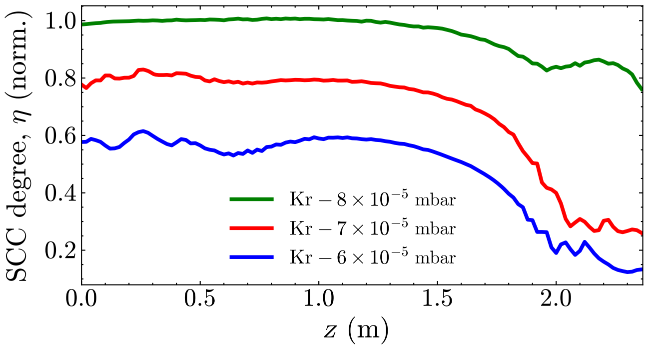

FIG. 10. SCC degree for different injected krypton gas pressures along the beamline.

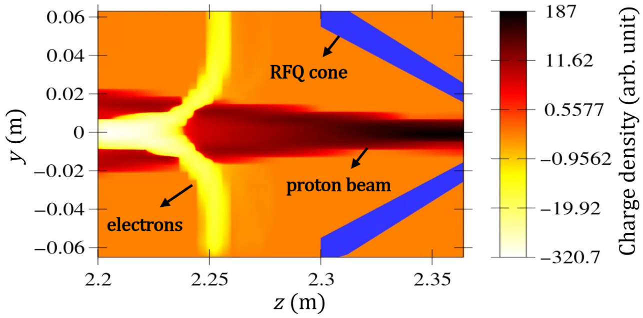

FIG. 11. A cone electrode positioned before the RFQ repels neutralizing particles into the LEBT. The colorbar distinguishes the proton beam and electron charge densities.

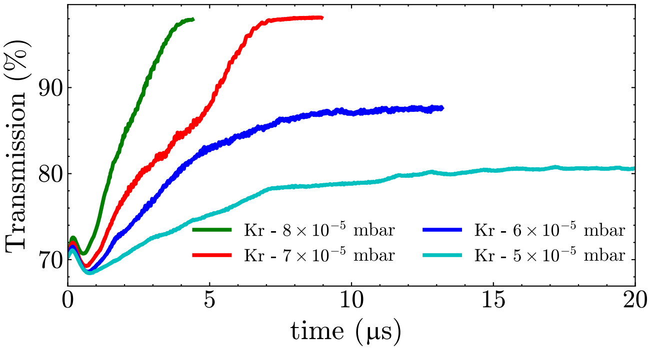

FIG. 13. Beam transmission evolution for injected krypton gas at different pressures.

particles from entering the RFQ. This configuration has the dual benefit of avoiding systematic errors in the measurement of the beam current and helping to maintain the compensation level [31]. In the figure, the proton beam enters the injection hole without distortion, while secondary electrons are repelled back to the LEBT when the applied cone voltage is around $V_{\mathrm{cone}} = -200$ V.

The effect of the cone potential on the SCC degree along the beamline is shown in Fig. 12. The result reveals how the cone potential influences the accumulation and distribution of compensating particles. When the cone potential is activated, the degree of space-charge compensation decreases more sharply near the entrance of the RFQ. This suggests that the negative cone potential is repelling a larger fraction of the compensating electrons, resulting in a more abrupt transition to an uncompensated beam. On the other hand, no significant changes in beam parameters are observed at the level of $V_{\mathrm{cone}} = -200$ V. This voltage is sufficient to prevent secondary electrons from entering the RFQ region, as their energies are typically much lower than this threshold.

C. Evaluation of beam parameters under SCC

In Sec. III B, we discussed the SCC model, analyzed the evolution of beam potential resulting from this effect, and examined the degree of SCC under various conditions. Now, we will evaluate the beam parameters during the SCC process. Since the time-resolved emittance measurements are conducted, we will present a detailed discussion of beam emittance evaluation and a comparison of numerical calculations with experimental results in Sec. IV. This section will specifically focus on how SCC impacts beam transmission and the rms beam size, which are essential indicators of beam stability and transport efficiency.

The changes in beam transmission and rms beam size during the build-up time with different pressures of injected krypton gas are illustrated in Figs. 13 and 14, respectively. In this example, we intentionally modeled the LEBT line with a beam transmission rate of approximately 70%, consistent with the transmission rate measured in the BTS beamline. For all gas pressures, the transmission rate increases over time because compensating electrons neutralize the beam's space charge, stabilizing after approximately 4–15 μs. Simultaneously, the rms beam size decreases over time. It is worth noting the transient reduction in transmission rate and the temporary increase in rms size at 1 μs. The principle is similar to that discussed in the previous section; accumulation of secondary ions occurs. During this period, the space-charge density increases due to ion accumulation and then gradually decreases as the ions are expelled radially from the beam.

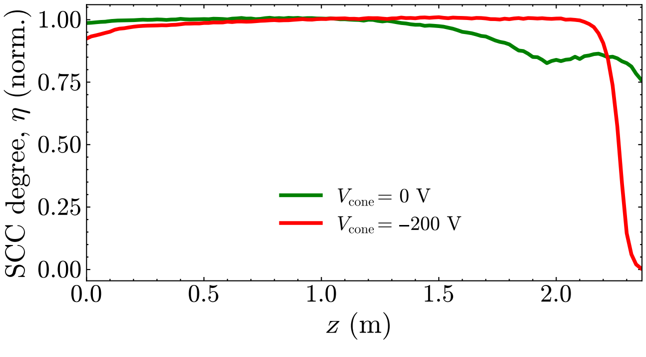

FIG. 12. A comparison of the SCC degree when the V_{cone} is turned off versus when it is activated.

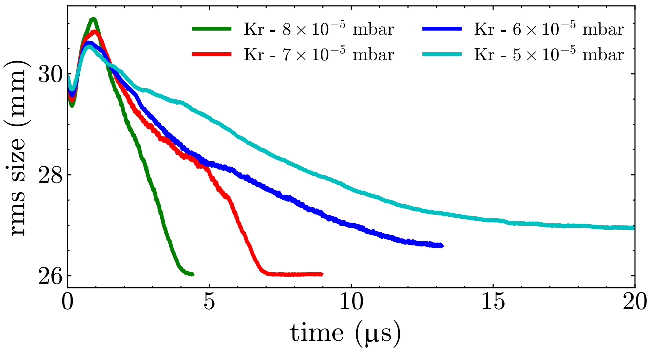

FIG. 14. The evaluation of rms beam size during the build-up time at different injected krypton pressures.

Higher gas pressures result in a higher final transmission rate and smaller rms size in the steady state.

IV. EXPERIMENTAL RESULTS

The layout of the KOMAC BTS experimental configuration is detailed in Sec. II B. The proton beam is extracted from a three-electrode microwave ion source with an energy of 25 keV, and pulse length of approximately 500 μs, providing sufficient time to perform time-resolved measurements. We can adjust the beam current levels between 12 and 20 mA while stable plasma conditions are maintained during beam extraction. Before conducting the phase-space measurement, a gate valve is positioned between the second solenoid magnet and the second ACCT to isolate the RFQ from the experimental line. The vertical and horizontal Allison scanners are capable of analyzing beam pulses with a resolution of 1 μs, enabling time-resolved phase-space measurements.

To account for uncertainties from the Allison scanner, we consider both systematic and statistical sources. Systematic uncertainties primarily arise from the step motor resolution, the geometrical structure of the scanner, and the nonlinearity of the electric field applied to the deflection electrodes. The overall position accuracy of the system remains within 1 mm, as the step motor provides better than 1 mm precision under the current scanner configuration. For angular measurements, the angular resolution of the Allison scanner is approximately 1.5 mrad. To avoid distortion due to oversampling beyond this resolution limit, we conduct measurements at intervals of approximately 2.3 mrad. In this setup, the gap between the deflection electrodes is 3.5 mm, and the beamlet, after passing through an initial slit with a width of 0.1 mm, enters the deflection region with a size significantly smaller than the electrode gap. As a result, the influence of fringe fields is considered negligible. We estimate statistical uncertainties based on signal noise levels and data fitting procedures applied to the measured phase-space profiles. For this purpose, we apply a density-based spatial clustering algorithm (DBSCAN) [32] to the raw phase-space measurements in order to eliminate noise and contributions from other species. By adjusting the clustering parameters, we successfully capture the full beam profile even when the phase-space distribution is nonuniform. Finally, we calculate the rms emittances based on the second moments of the filtered position and angle distributions.

Argon and krypton gases are injected into the beamline right after the ion source and before the first ACCT. This setup also allows us to evaluate beam losses at the beginning of LEBT based on the gas injection pressure. A vacuum gauge is installed at the same longitudinal position as the Allison scanner, ensuring accurate measurement of the gas pressure at the location where phase-space measurements are performed. Before gas injection, the baseline pressure in the beamline is maintained at approximately 2.5×10^{-5} mbar. We gradually injected argon and krypton gases separately and conducted phase-space measurements at specific pressure levels. For each gas, the appropriate gas correction factor is applied to account for differences in the ionization factors of argon and krypton, allowing us to obtain the corrected pressure value. Specifically, ionization gauges are typically calibrated for nitrogen and therefore exhibit different sensitivities when used with other gases. To correct this, we applied standard correction factors: 1.29 for argon and 1.94 for krypton. These factors account for the lower ionization efficiencies of these noble gases compared to nitrogen. As a result, the actual gauge reading is divided by the appropriate gas correction factor to get the corrected pressure value for the specific gas being measured.

A. Time-resolved phase-space measurement

Time-resolved transverse emittance measurement for different injected krypton gas pressure levels is presented in Fig. 15. The steady state time for the 15 mA extracted beam current as a function of krypton pressure is compared, reflecting the dynamics of SCC over the formation process of the beam. The "base" case refers to the pressure level at which no gas injection has yet occurred in the figure. The other two lines indicate the krypton pressure level, considering the gas correction factor. The higher emittance values at these peak points indicate that the beam is still in its early formation stage. The time it takes for the beam to stabilize and reach a steady state depends on the krypton pressure, with higher pressures accelerating the process.

Furthermore, we need to examine the comparison between numerical and experimental rising times. Specifically, as illustrated in Fig. 7, the numerical rising time is shorter than the measured build-up time from the experiment given in Fig. 15. This indicates a potential discrepancy between theoretical predictions and empirical results, emphasizing the importance of understanding the factors that may contribute to this difference. One such factor is discussed in Ref. [33], which found that the

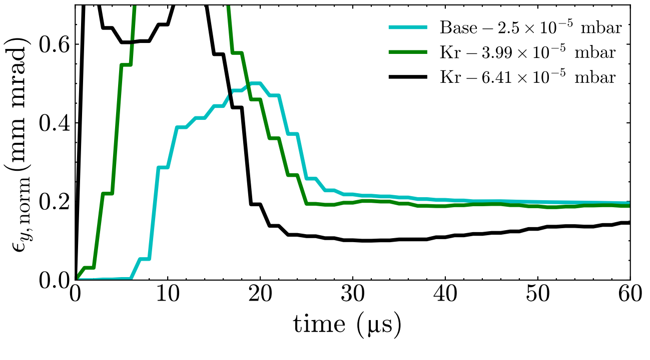

FIG. 15. The experimental comparison of the steady state time for different krypton and base pressure levels. The extracted beam current is 15 mA.

experimental rise time differs from the theoretical value by a factor of 2. The minimum rise time is calculated under the assumption that electron losses are negligible. However, in reality, not all electrons contribute to the compensation; those with higher kinetic energy may escape from the beam. In our case, the discrepancy is even greater, with the experimental rise time being 4 to 5 times longer than the simulated value. This larger deviation may be attributed to additional factors such as uncertainties in the high-voltage switch rise time during beam extraction, as well as the characteristics of the initial free electron velocity used in the simulation model during impact ionization.

The efficiency of different types of injected gases is evaluated through both numerical simulations and experiments. Numerical calculations, as shown in Fig. 8, reveal that krypton is more effective than argon in promoting SCC under identical conditions. To support these findings, experimental measurements were conducted using the same initial beam parameters, which resulted in very similar equilibrium emittances across the different cases. Figure 16 presents the evolution of the normalized transverse emittance over time for both krypton and argon gases at two distinct pressure levels (3.06×10^{-5} mbar and 4.45×10^{-5} mbar). Two gas controllers are employed to inject the gases separately, with krypton being injected first. This approach is taken because the argon gas controller is more flexible in achieving the same pressure level as that of krypton. The results demonstrate that krypton exhibits a faster build-up of SCC and earlier stabilization of emittance compared to argon, highlighting its greater efficiency in neutralizing space charge.

The numerical results shown in Fig. 9 demonstrate that as the beam current decreases, the compensation time increases. To experimentally examine this behavior, we performed time-resolved experiments under similar conditions, examining the effects of varying beam currents on the compensation process. Figure 17 highlights the dependence of transverse emittance evolution on beam current under SCC conditions. The measurements are taken at a krypton pressure of approximately 5.3×10^{-5} mbar. It is important to note that the experimental conditions, including beam energy, LEBT solenoid settings, and base pressure levels, remain consistent across all measurements. The variations in beam current are entirely attributable to the solenoid magnet and microwave power settings of the ion source. For the 17 mA case, the emittance stabilizes quickly and reaches a lower steady state value, while for the beam with 12 mA, the emittance stabilizes more slowly and ends at a noticeably higher final value. One contributing factor to these differences is the beam current, but another significant factor is the beam size. An increase in the beam size may slow down the SCC process due to enhanced electron losses [24]. It is obvious that the emittance value for the 12 mA beam is significantly higher than the emittance values of the other two results. The experimental setup was optimized specifically for the 15 mA beam, and no recalibration was performed when the beam current was reduced to 12 mA. As a result, the solenoid settings did not adequately match the lower-current beam, leading to increased divergence and higher beam size.

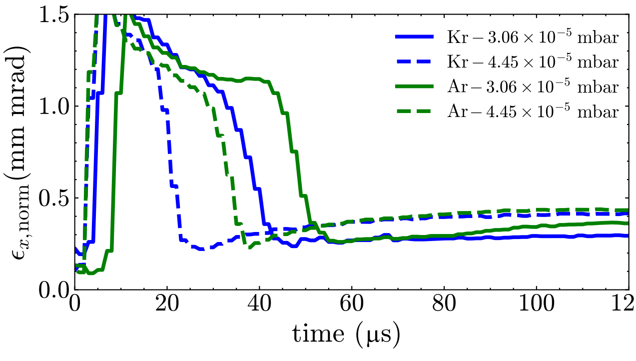

FIG. 16. Experimental results of normalized transverse emittance as a function of time for different injected gases in different pressures. The extracted beam current is 13.2 mA.

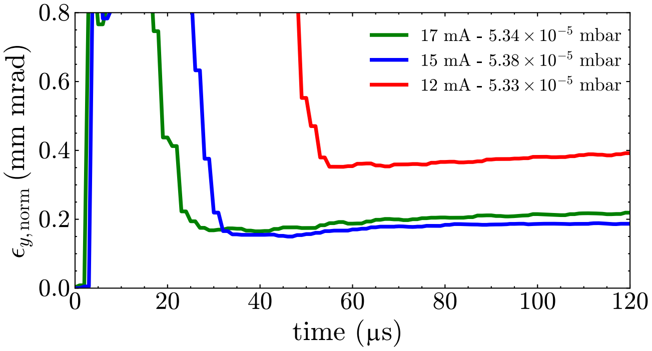

FIG. 17. Measured normalized emittance values for different beam currents over time. The current values correspond to the baseline case (before gas injection), assuming no beam losses, while the pressure levels represent krypton pressures.

B. Nonlinearities and emittance growth

Beams injected into a linear transport channel typically have some degree of space-charge nonuniformity. Numerical calculations show that the nonlinear space-charge effect of a bunched beam in a linac is one of the primary reasons for emittance growth [34]. To investigate the impact of SCC on these nonlinear effects, phase-space measurements are taken before and after gas injection, enabling a direct comparison of the beam's uniformity.

Figure 18 illustrates both experimental and simulation results of the beam's phase-space distribution under baseline pressure conditions and at the steady state. The analysis reveals how nonlinear space-charge effects and beam nonuniformity contribute to emittance change. In this configuration, the baseline pressure is 2.5×10^{-5} mbar,

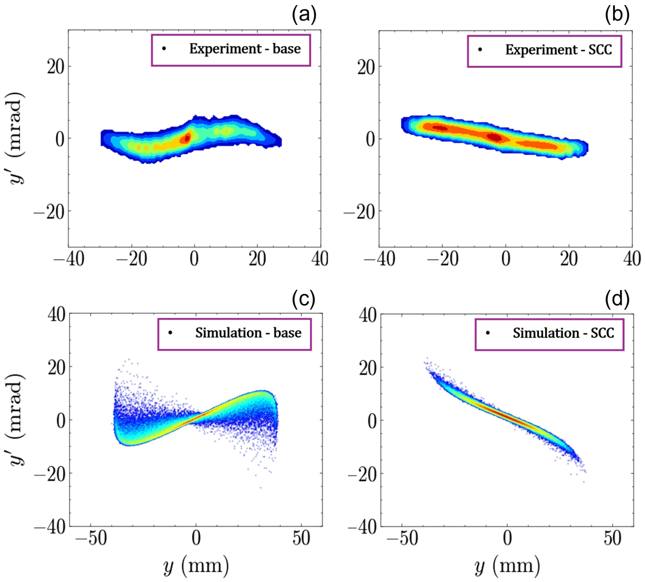

FIG. 18. Phase-space distribution of the beam before and after injection of argon, showing both experimental (top) and simulation (bottom) results. The beam current is at the 15 mA level.

while the pressure level with argon is 3.5×10^{-5} mbar. In the experimental base case [Fig. 18(a)], the beam shows significant distortion in phase space, which indicates the nonuniform density that likely arises due to aberrations in the ion optical system. A similar phenomenon is observed in the simulation [Fig. 18(c)], as the initial phase distribution is derived from the results of the simulated ion source. After SCC [Figs. 18(b) and 18(d)], the distribution becomes more focused and linear, demonstrating how SCC mitigates nonuniformity and stabilizes the beam, resulting in a reduction of emittance. Another notable outcome of SCC is the convergence of the beam. As the space charge decreases through SCC, the beam becomes more convergent with the same solenoid magnet settings, which is consistent with expectations.

On the other hand, increasing pressure level changes the dynamics of the phase-space distribution. Figure 19 illustrates the normalized transverse emittance growth rate as a function of gas pressure, comparing both simulated krypton results and experimental measurements with krypton and argon injection at steady state conditions. Experimental and calculated baseline normalized emittance values are 0.213 and 0.350 mm mrad, respectively, at a pressure level of approximately $\sim 2.5 \times 10^{-5}$ mbar. While lower pressures contribute to more efficient SCC, the data indicate that increasing pressure levels introduce new nonlinearity effects that lead to emittance growth. In the low-pressure region ($3 \times 10^{-5} - 4 \times 10^{-5}$ mbar) the emittance remains relatively stable for both krypton and argon measurements. However, at higher pressures, a more pronounced emittance growth is observed, surpassing the baseline value. We observe a similar trend in the simulation results. As shown in the figure, the emittance growth rate begins to increase beyond a pressure level of 6×10^{-5} mbar. This increase is attributed to the excitation of new nonlinearities in the system. At higher pressure levels, the central region of the beamline becomes nearly fully neutralized due to effective space-charge compensation. However, the entrance and exit regions of the beamline remain only partially compensated, creating spatial gradients in the compensation level. These nonuniformities contribute to emittance growth. Nevertheless, in the simulation, we observe that the emittance growth rate remains below the baseline value.

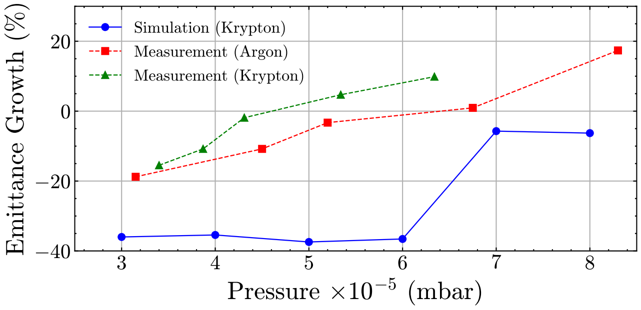

FIG. 19. Normalized transverse emittance rate as a function of pressure for both simulation and experimental measurements. The base pressure level is around $\sim 2.5 \times 10^{-5}$ mbar.

C. Impact of SCC on RFQ matching

Proper matching of the beam's properties to the RFQ input is critical for achieving high transmission efficiency and maintaining beam quality. The two solenoid magnets in the LEBT line are tuned to match the beam's transverse properties to the RFQ entrance. Before evaluating the numerical SCC dynamics, solenoid adjustments are made to optimize the RFQ matching conditions. When SCC is introduced, the effective space charge of the beam changes, altering its dynamics. If the solenoid settings remain unchanged, the beam may become mismatched, even with improved phase- space distribution due to SCC. An example is shown in Fig. 20 to illustrate the phase-space

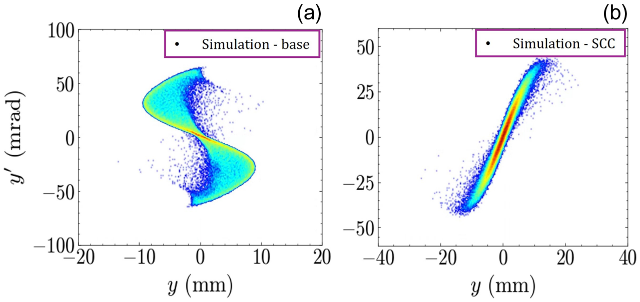

FIG. 20. Simulation results of the phase-space distribution at the end of the LEBT line, before (a) and after (b) the establishment of SCC.

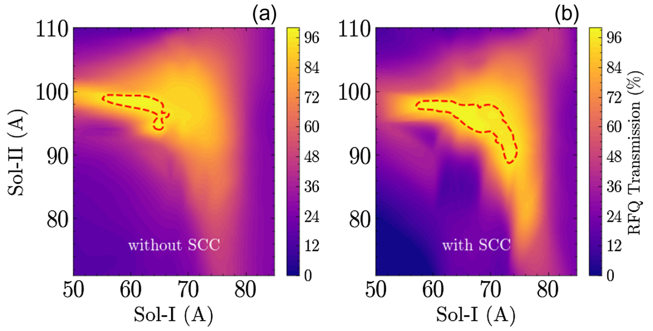

FIG. 21. RFQ transmission efficiency as a function of the current settings for the two solenoid magnets. Left: during the stage of no injected gas. Right: in the steady state condition after the injection of argon gas. The color map represents the RFQ transmission efficiency, with the dashed red lines marking regions where the transmission exceeds 95%.

distribution of the beam at the entrance of the RFQ. The left-hand figure, labeled "Simulation-base" represents the uncompensated beam, while the right-hand figure, labeled "Simulation-SCC" reflects the beam behavior after the neutralization of the space charge. These distributions highlight conditions in beam matching to the RFQ and the potential mismatch caused by unchanged solenoid magnet settings when SCC is introduced.

To assess the impact of SCC on RFQ transmission efficiency, the RFQ is integrated into the experimental setup by opening the gate valve located between the second solenoid magnet and the second ACCT. Figure 21 illustrates the transmission efficiency as a function of the LEBT line solenoid magnets' current settings. As observed in Fig. 21(a), the RFQ transmission is more efficient when the Solenoid-II current is around 100 A. In contrast, in Fig. 21(b), where the argon gas is inserted, the transmission becomes more efficient when the Solenoid-II current is reduced to below 100 A. This behavior is consistent with our expectations: the beam becomes less divergent as SCC mitigates space-charge effects. Consequently, the solenoid strength must be reduced to appropriately focus and match the beam to the RFQ entrance. This adjustment ensures optimal beam transport and high transmission efficiency.

V. CONCLUSION

This study provides an investigation into the dynamics and optimization of space-charge compensation in the low-energy beam transport of a high-perveance proton beam system. Through a combination of detailed 3D numerical simulations and time-resolved measurements, the research clarifies the key factors that influence the build-up time and efficiency of SCC, as well as its impact on beam quality.

In the numerical calculations, the dynamics of secondary ions were analyzed in detail, with particular attention given to their expulsion from the beam. Secondary ions, which are produced alongside secondary electrons during the gas ionization process, significantly influence the build-up time. By incorporating ion dynamics into the simulation, it was observed that the build-up time increases due to the mobility of the ions and their contribution to the potential evolution.

The experimental data show good agreement with the simulation in terms of overall trends in SCC dynamics across various operating conditions, supporting the reliability of the numerical model. Key parameters, including gas type, injection pressure, and beam current, were systematically analyzed, and time-resolved experiments were conducted to validate the numerical findings. The results emphasize these parameters' critical role in the SCC process, particularly for short-pulse beam operation, where understanding the beam formation time is essential. Krypton consistently showed faster SCC build-up times compared to argon, and both time-resolved measurements and simulations supported this observation. However, some discrepancies between theoretical predictions and experimental results were observed, particularly in the compensation time. The experimental build-up times were consistently longer than the theoretical estimates, likely due to factors such as the electron loss mechanism and the rising time of the ion source high-voltage switch. In terms of the rise time effect, it is difficult to quantify precisely due to fluctuations observed in the beam's rising edge, which typically occur in the range of $10 - 30$ μs. Although we do not have direct measurements of the high-voltage rise time precisely, we anticipate that this rising period contributes to the gradual formation of the beam.

Higher beam currents result in a larger initial potential due to stronger space charge, but they also reach the SCC characteristic time more quickly. This faster compensation is attributed to an increased production of secondary particles and the quicker expulsion of ions. This illustrates the direct effect of beam current on the dynamics of space-charge compensation. Measurements show a consistent trend in which the time required for space-charge compensation decreases as the beam current increases, in general agreement with the behavior predicted by simulations.

The charge distribution within the beam is inherently nonuniform due to nonlinear space-charge forces, as shown in the simulation and experimental results. This leads to significant phase-space distortion, as observed in the uncompensated case. SCC reduces the intensity of the nonlinear forces acting on the beam, leading to a more uniform phase-space distribution and improved stability and focus. Despite the SCC, some emittance growth persists due to nonlinearities at high-pressure levels. It is, therefore, crucial to adjust SCC parameters carefully, such as injected gas pressure, to achieve optimal results.

The investigation of the RFQ transmission with injected gas highlights the necessity of reoptimizing solenoid magnet settings to accommodate SCC-induced changes in beam dynamics, ensuring proper RFQ matching and high transmission efficiency. The reduced space-charge forces require lower solenoid strengths to maintain optimal beam focusing and RFQ matching. The numerical model and its dedicated validation through actual experiments presented in this study will be of significant importance for the design and operation of future high-power accelerators with considerably high space charge.

ACKNOWLEDGMENTS

This work was supported by the National Research Foundation of Korea (NRF), funded by the Ministry of Science and ICT (MSIT) of the Republic of Korea (NRF-2020R1A2C1010835, RS-2025-00563391, and KAERI-524320-25), including support through the KOMAC operation fund of KAERI.

DATA AVAILABILITY

The data that support the findings of this article are not publicly available. The data are available from the authors upon reasonable request.

APPENDIX: KINEMATICS OF IMPACT IONIZATION

When a charged particle passes through a neutral gas, it can interact with the bound electrons of the atoms or molecules in the gas. The proton may transfer energy to a bound electron. If the transferred energy is sufficiently high, the electron may be ejected from the atom, leading to ionization.

The overall reaction can be described as

$$\mathrm{H}^+ + \mathrm{X} \rightarrow \mathrm{H}^+ + \mathrm{X}^+ + e^-, \tag{A1}$$

where X is a neutral atom, X^+ is the resulting ion, and e^- is the free electron. For ionization to occur, the energy ΔE transferred from the proton to the electron must exceed the ionization potential U_i of the atom [35,36]:

$$\Delta E > U_i. \tag{A2}$$

Here, U_i represents the minimum energy required to liberate the electron from its bound state. For example, the ionization energy of argon is 15.76 eV, and that of krypton is 13.9996 eV, as reported by the NIST Atomic Spectra Database [37]. The maximum possible energy that can be transferred in a two-body elastic collision between a proton (mass m_p) and an electron (mass m_e) is given by

$$\Delta E_{\max} = K_{12} E_p, \tag{A3}$$

where the dimensionless mass-transfer coefficient K_{12} is defined as

$$K_{12} = \frac{4 m_e m_p}{(m_e + m_p)^2}. \tag{A4}$$

Due to the large mass difference ($m_p \gg m_e$), this factor is small, and only a small fraction of the proton's energy can be transferred to the electron. The energy transferred in excess of the ionization potential becomes the kinetic energy of the ejected (free) electron:

$$E = \Delta E - U_i. \tag{A5}$$

This energy E is observable and determines the velocity and energy distribution of the emitted electron. For example, when a 25 keV proton beam ionizes argon or krypton atoms, the maximum observable electron energies, using Eq. (A5), are: $E_{\mathrm{Ar}} = 54.5\ \mathrm{eV} - 15.76\ \mathrm{eV} = 38.74\ \mathrm{eV}$ and $E_{\mathrm{Kr}} = 54.5\ \mathrm{eV} - 13.9996\ \mathrm{eV} = 40.50\ \mathrm{eV}$.

[1] R. Gobin, P.-Y. Beauvais, R. Ferdinand, P.-A. Leroy, L. Celona, G. Ciavola, and S. Gammino, Improvement of beam emittance of the CEA high intensity proton source SILHI, Rev. Sci. Instrum. **70**, 2652 (1999).

[2] P. Beauvais, R. Ferdinand, R. Gobin, J. Lagniel, P.-A. Leroy, L. Celona, G. Ciavola, S. Gammino, B. Pottin, and J. Sherman, Emittance improvement of the electron cyclotron resonance high intensity light ion source proton beam by gas injection in the low energy beam transport, Rev. Sci. Instrum. **71**, 1413 (2000).

[3] A. Jakob, H. Klein, A. Lakatos, O. Meusel, and J. Pozinski, Time-resolved investigation of the compensation process of pulsed ion beams, in *Proceedings of the 1999 Particle Accelerator Conference* (IEEE, 1999), Vol. 3, pp. 1836–1838, https://cds.cern.ch/record/553591/files/tup146.pdf.

[4] A. Jakob, P. Y. Beauvais, R. Gobin, H. Klein, J. L. Lemaire, P. A. Leroy, and J. Pozimski, Time-resolving diagnostic of the compensation process of pulsed ion beams at high-intensity light ion source, Rev. Sci. Instrum. **71**, 1107 (2000).

[5] A. Jakob, H. Klein, A. Lakatos, J. Pozimski, and L. Wicke, Investigation of the rise of compensation of high perveance ion beams using a time-resolving ion energy spectrometer, in *Proceedings of the 6th European Particle Accelerator Conference (EPAC 1998)* (2005), https://accelconf.web.cern.ch/e98/PAPERS/WEP07A.PDF.

[6] T. Weis, R. Dölling, P. Gross, H. Klein, and J. Wiegand, Space-charge neutralization in low-energy beam lines, Nucl. Instrum. Methods Phys. Res., Sect. A **278**, 224 (1989).

[7] I. Soloshenko, Physics of ion beam plasma and problems of intensive ion beam transportation (invited), Rev. Sci. Instrum. **67**, 1646 (1996).

[8] I. Soloshenko, Space charge compensation of technological ion beams, in *Proceedings of the 18th International Symposium on Discharges and Electrical Insulation in Vacuum (ISDEIV)* (1998), Vol. 2, pp. 675–678, https://ieeexplore.ieee.org/document/738839.

[9] D. Winklehner, D. Leitner, D. Cole, G. Machicoane, and L. Tobos, Space-charge compensation measurements in electron cyclotron resonance ion source low energy beam

transport lines with a retarding field analyzer, Rev. Sci. Instrum. **85**, 02A739 (2014).

[10] D. Winklehner and D. Leitner, A space charge compensation model for positive DC ion beams, J. Instrum. **10**, T10006 (2015).

[11] M. D. Gabovich, Ion-beam plasma and the propagation of intense compensated ion beams, Phys. Usp. **20**, 134 (1977).

[12] D. Gabor, A space-charge lens for the focusing of ion beams, Nature (London) **160**, 89 (1947).

[13] O. Meusel, M. Droba, D. Noll, K. Schulte, P. P. Schneider, and C. Wiesner, Beam transport and space charge compensation strategies, Rev. Sci. Instrum. **87**, 02B937 (2016).

[14] V. Shiltsev, New possibilities for beam-beam and space-charge compensation: MCP gun and electron columns, in *Proceedings of the 2007 IEEE Particle Accelerator Conference (PAC)* (IEEE, 2007), pp. 1159–1160, https://ieeexplore.ieee.org/document/4441015.

[15] C. S. Park, B. Freemire, M. Chung, G. Stancari, and E. Stern, Progress in space charge compensation using electron columns, J. Instrum. **16**, P03048 (2021).

[16] A. Oeftiger and O. Boine-Frankenheim, Pulsed electron lenses for space charge mitigation, Phys. Rev. Lett. **132**, 175001 (2024).

[17] P. W. Allison, J. D. Sherman, and D. B. Holtkamp, An emittance scanner for intense low-energy ion beams, IEEE Trans. Nucl. Sci. **30**, 2204 (1983).

[18] M. Reiser, *Theory and Design of Charged Particle Beams*, 2nd ed. (John Wiley & Sons, 2008), 10.1002/9783527622047.

[19] A. Holmes, Theoretical and experimental study of space charge in intense ion beams, Phys. Rev. A **19**, 389 (1979).

[20] M. E. Rudd, Y.-K. Kim, D. H. Madison, and J. W. Gallagher, Electron production in proton collisions: Total cross sections, Rev. Mod. Phys. **57**, 965 (1985).

[21] M. E. Rudd, Y.-K. Kim, D. H. Madison, and T. J. Gay, Electron production in proton collisions with atoms and molecules: Energy distributions, Rev. Mod. Phys. **64**, 441 (1992).

[22] E. Cosgun, S. Moon, D. Kim, and M. Chung, Studies of space-charge compensation of positive ions by creating time-dependent secondary electrons in low-energy beam transport line, in *Proceedings of the 15th International Particle Accelerator Conference (IPAC '24), Nashville, TN USA* (JACoW, Geneva, Switzerland, 2024), pp. 201–203, 10.18429/JACoW-IPAC2024-MOPC61.

[23] N. Chauvin, O. Delferrière, R. Duperrier, R. Gobin, P. A. P. Nghiem, and D. Uriot, Transport of intense ion beams and space charge compensation issues in low energy beam lines, Rev. Sci. Instrum. **83**, 02B320 (2012).

[24] A. BenIsmail, R. Duperrier, D. Uriot, and N. Pichoff, Space charge compensation studies of hydrogen ion beams in a drift section, Phys. Rev. ST Accel. Beams **10**, 070101 (2007).

[25] C. A. Valerio-Lizarraga, I. Leon-Monzon, and R. Scrivens, Negative ion beam space charge compensation by residual gas, Phys. Rev. ST Accel. Beams **18**, 080101 (2015).

[26] S. X. Peng, A. L. Zhang, H. T. Ren, T. Zhang, J. F. Zhang, Y. Xu, J. M. Wen, W. B. Wu, Z. Y. Guo, and J. E. Chen, Study on space charge compensation of low energy high intensity ion beam in Peking University, in *Proceedings of the 57th ICFA Advanced Beam Dynamics Workshop on High-Intensity and High-Brightness Hadron Beams (HB2016), Malmö, Sweden* (JACoW, Geneva, Switzerland, 2016), pp. 453–457, 10.18429/JACoW-HB2016-WEPM6Y01.

[27] F. Gérardin, M. Baylac, D. Bondoux, F. Bouly, A. Chancé, N. Chauvin, O. Napoly, N. Pichoff, D. Uriot *et al.*, Space charge compensation in low energy beam lines, in *Proceedings of the 7th International Particle Accelerator Conference (IPAC'16), Busan, Korea* (JACoW, Geneva, Switzerland, 2016), pp. 3055–3057, 10.18429/JACoW-IPAC2016-WEPOY033.

[28] C. A. Valerio-Lizarraga, J.-B. Lallement, I. Leon-Monzon, J. Lettry, Ø. Midttun, and R. Scrivens, Space charge compensation in the Linac4 low energy beam transport line with negative hydrogen ions, Rev. Sci. Instrum. **85**, 02A505 (2014).

[29] T. Kalvas, O. Tarvainen, T. Ropponen, O. Steczkiewicz, J. Ärje, and H. Clark, IBSimu: A three-dimensional simulation software for charged particle optics, Rev. Sci. Instrum. **81**, 02B703 (2010).

[30] N. Chauvin, Space-charge effect, arXiv:1410.7991.

[31] D. Noll, R. A. Baron, C. S. Derrez, E. M. Donegani, M. Eshraqi, F. Grespan, H. Hassanzadegan, B. Jones, Y. Levinsen, N. Milas, R. Miyamoto, C. Plostinar, A. Garcia Sosa, and R. Zeng, First beam matching and transmission studies on the ESS RFQ, in *Proceedings of the 31st International Linear Accelerator Conference (LINAC'22)* (JACoW, Geneva, Switzerland, 2022), pp. 414–417, 10.18429/JACoW-LINAC2022-TUPOPA04.

[32] E. Schubert, J. Sander, M. Ester, H.-P. Kriegel, and X. Xu, DBSCAN revisited, revisited: Why and how you should (still) use DBSCAN, ACM Trans. Database Syst. **42**, 19 (2017).

[33] A. Jakob, R. Dölling, K. Reidelbach, J. Pozimski, and H. Klein, Investigation of the space-charge compensation process of ion beams using a time-resolving ion energy spectrometer, Nucl. Instrum. Methods Phys. Res., Sect. A **415**, 490 (1998).

[34] Y. Chen and Z. Huang, Nonlinear space charge effects and emittance growth in LINAC, Chin. Phys. C **23**, 1231 (1999), https://hepnp.ihep.ac.cn/en/article/id/f4f2c55d-ac34-418f-9d7d-50b4d670c928.

[35] L. R. Evans and D. J. Warner, Space-charge neutralisation of intense charged particle beams : Some theoretical considerations, Technical Report No. CERN-MPS-LIN-71-2, CERN, Geneva, 1971, https://cds.cern.ch/record/2853786.

[36] M. Gryziński, Classical theory of electronic and ionic inelastic collisions, Phys. Rev. **115**, 374 (1959).

[37] A. Kramida, Y. Ralchenko, J. Reader, and N. A. Team, NIST atomic spectra database (ver. 5.12), 2024, available at https://physics.nist.gov/asd [accessed: 2025-05-10].